





Article

New Perspective on Thermally Stimulated Luminescence and Crystallization of Barium Borate Oxyfluoride Glasses

Mauricio Rodríguez Chialanza ^{1,2,*} , Germán Azcune ³ , Heinkel Bentos Pereira ³  and Ricardo Faccio ⁴ 

¹ PDU Ciencias Físicas y sus Aplicaciones, Centro Universitario Regional del Este (CURE), Udelar, Rocha 2700, Uruguay

² GDMEA, Área Radioquímica, Facultad de Química, Udelar, Montevideo 11800, Uruguay

³ GDMEA, Centro Universitario Regional del Este (CURE), Udelar, Rocha 2700, Uruguay; german.azcune@gmail.com (G.A.); yandinoca@gmail.com (H.B.P.)

⁴ Área Física & Centro NanoMat, DETEMA, Facultad de Química, Udelar, Montevideo 11800, Uruguay; rfaccio@fq.edu.uy

* Correspondence: mrodriguez@cure.edu.uy

Abstract: The demand for modern materials, especially glasses, used in different applications, such as radiation sensors and spectral converters, requires a detailed study of their properties. The incorporation of fluoride compounds in borate glasses and their crystallization at the nanometric scale allows the properties of these materials to be further enhanced. Although many works showed improvements in some of these properties, some critical aspects, such as the crystallization mechanism and the role of the fluorine phase, need more investigation. We worked with $x\text{NaF} (100 - x)\text{BaO} \cdot 2\text{B}_2\text{O}_3$ glasses with $x = 0, 5, 10, 15, 20, 25, 30,$ and 35% (in mol) to increase the knowledge in this field. The structural modifications and the thermally stimulated luminescence of the glasses were studied, and their crystallization was analyzed by thermal analysis and X-ray diffraction. A continuous trap distribution was found, which was responsible for its very good luminescent signal, especially in glasses with 20% NaF. By selecting a suitable amount of NaF, it is possible to obtain nanocrystals of BaF_2 . These promising results we reached show the applicability of these materials.

Keywords: oxyfluoride; borates; nanocrystals



Citation: Rodríguez Chialanza, M.; Azcune, G.; Bentos Pereira, H.; Faccio, R. New Perspective on Thermally Stimulated Luminescence and Crystallization of Barium Borate Oxyfluoride Glasses. *Crystals* **2021**, *11*, 745. <https://doi.org/10.3390/cryst11070745>

Academic Editors: Araceli De Pablos Martin and Giulio Gorni

Received: 30 April 2021

Accepted: 14 June 2021

Published: 26 June 2021

Publisher's Note: MDPI stays neutral with regard to jurisdictional claims in published maps and institutional affiliations.



Copyright: © 2021 by the authors. Licensee MDPI, Basel, Switzerland. This article is an open access article distributed under the terms and conditions of the Creative Commons Attribution (CC BY) license (<https://creativecommons.org/licenses/by/4.0/>).

1. Introduction

Thermally stimulated luminescence or thermoluminescence (TL) is being actively studied for different reasons; one of them has to do with practical purposes, that is, for the development of materials that can be used in dosimetry applications [1]. It is also used, with the aid of optical absorption emission and excitation spectroscopy, to study the mechanisms of luminescence in different materials [2] and for the study of defects in crystals [3] and dating purposes, among other studies [4].

In particular, in recent times, attention has been paid to borate crystals [5] and glasses [6] because they present optimal dosimeter application conditions. It is expected that, in order to improve the response and sensitivity to radiation of glasses, various strategies are used, such as those doped with transition metals [7] and rare earths [8], the combination of various modifying elements [9] and various glass formers [10], and even glass crystallization [11].

Another strategy to improve the luminescent response and its sensitivity is incorporating a fluoride compound in the glass matrix, reducing the phonon energy of the system. This strategy was used to improve up-conversion phenomena in many glass systems [12]. The incorporation of fluoride compounds in silicate glass and the crystallization of nanometric particles in the glass matrix allowed an increase in luminescence and crystallization, which is well documented in many reviews [13,14]. One of the possibilities of forming these crystalline nanoparticles in the glass matrix consists of a phase separation process in

the glass matrix that produces a variation in the concentration of some components around the phase separation droplets. The increase in Si content around the droplet produces a modification in the viscosity at the droplet interface, producing a higher diffusion barrier and a limitation in the crystal growth, which results in a uniform distribution of the size of the nanocrystals in the glass matrix [15]. By proper selection of the glass composition, the fluoride compound is limited to crystallize in the droplet. These nanometric-sized crystals have low phonon energy and, as they are nanometric, the glass-ceramic maintains its transparency and shows better luminescence [16]. The improvements in luminescence due to the crystallization of the fluoride phase were observed in other glass systems, such as germanite [17], phosphate [18] and borate [19]. However, the crystallization of the fluoride phase is not well understood in borate glasses. Recently, it was suggested that, due to the low viscosity of borate glass compared to silicate, there would be no diffusion barrier. As there is no diffusion barrier, the growth of the crystals would not be limited and therefore this would not be the explanation for obtaining nanocrystals. Consequently, these authors suggest that the nanoscale crystal growth would be mainly due to an increase in the nucleation rate when doping the matrix with Er^{3+} [20].

Based on the above, and considering that incorporation of a fluoride compound can improve the luminescent properties, it is proposed to study the TL of an oxyfluoroborate glass. Based on previous results, $\text{BaO} \cdot 2\text{B}_2\text{O}_3$ glass has been chosen as the starting point [21]. Different amounts of NaF was incorporated into this glass, and a structural, thermal, and TL analysis was carried out. This work seeks to contribute to the structure's knowledge, crystallization, mechanism, and luminescent properties.

2. Materials and Methods

2.1. Glass Samples Preparation

Glass samples, with composition $x\text{NaF} \cdot (100 - x)\text{BaO} \cdot 2\text{B}_2\text{O}_3$ with $x = 0, 5, 10, 15, 20, 25, 30,$ and 35% (in mol) were prepared by the melt/quenching method using an electric furnace. Appropriate amounts of BaCO_3 , H_3BO_3 , and NaF were mixed using a high-speed ball mill. All reactants were ACS grade (purity > 99.5%, Merck KGaA, Darmstadt, Germany). The mixture powder was fused at $1100\text{ }^\circ\text{C}$ in a platinum crucible for 5 min to achieve a homogeneous liquid and avoid fluorine loss. Once the fusion was finished, the liquid was cast into a steel mold at room temperature. All the glass samples were heat treated to release stress before any characterization. For characterization, powder samples were obtained using an agate mortar and a high-speed ball mill. After that, powder glass samples were sieved according to different characterization samples. On the other hand, for density measurements, bulk samples were used.

2.2. Characterization

The FTIR spectroscopy technique was used to analyze possible structure variations. Powder glass samples were mixed with KBr (10% of samples) and pressed at 10 Ton. The FTIR spectra were recorded in the $400\text{--}4000\text{ cm}^{-1}$ wave-number range in a PerkinElmer Frontier (Shelton, CT, USA) spectrometer at room temperature. The spectra were obtained using an average of 60 scans per sample and normalized in the range $400\text{--}1600\text{ cm}^{-1}$. The analysis of the FTIR signal was performed using Origin software.

A WITec Alpha 300RA Confocal Raman Microscopy (Ulm, Baden-Wurtemberg, Germany) was used to measure the Raman spectra of the powder glass samples, utilizing a laser with an excitation wavelength of 532 nm. In total, 100 scans were averaged 0.1 s each and were normalized for comparison. A region between $400\text{--}1800\text{ cm}^{-1}$ was selected for interpretation.

Density measurements were performed using Archimedes' principle. A Mettler Toledo, ML204T, analytical balance equipped with a density accessory, was used. All measurements were done at room temperature, using water as an immersion liquid. The experimental error was $\pm 0.02\text{ gm/cm}^3$.

Differential scanning calorimetry (DSC) technique was used to evaluate thermal properties, such as glass transition temperature (T_g) and the onset temperature at the peak (T_c). All measurements were performed using a simultaneous thermal analysis (STA) 449F5 from Netzsch Geratebau GMBH (Selb, Germany). Powder samples between 25–45 μm particle size were used. Samples were heated using different heating rates: 5, 10, 20, and 30 K/min. Kinetic analysis was performed using the Kissinger method [22]. Using this method, we assume that crystallization occurs from a constant number of nuclei [23]. In our case, we are using particles, so we are also assuming that crystallization occurs mainly on the particles' surface, which allows us to make comparisons with other previously published work on $\text{BaO}\cdot 2\text{B}_2\text{O}_3$ glasses [21].

Polished to optical quality bulk samples were heat treated at different temperatures and times according to DSC data to analyze the crystalline phases. X-ray analysis was done using a Malvern Panalytical Diffractometer (Almelo, The Netherlands), Empyrean model, equipped with a copper tube, operating at 40 kV and 40 mA, using a Ni filter, Bragg–Brentano (θ – 2θ) geometry, a 1D mode Xcelerator detector, and $0.02^\circ/\text{min}$ per step. The Open Crystallographic Database was used as a database of crystalline phases [24].

Thermoluminescence (TL) measurements were done using RISØ DA-20 (DTU Nutech) TL/OSL equipment (Roskilde, Denmark), according to our previous publication [25]. All measurements were done at a 5.0 K/s heating rate and under a N_2 atmosphere. A $^{90}\text{Sr}/^{90}\text{Y}$ beta emitter, with maximum energy of 2.27 MeV and a nominal activity of 1.48 Gbq, was used as an irradiating source. The irradiation time was 7, 20, 34, 61, 102, 122, and 134 s, corresponding to nominal doses of 1, 3, 5, 9, 15, 18, and 20 Gy. Powder glass between the 150–250 μm range was used. Six aliquots for each sample were measured and then averaged for data analysis. We followed the recommendation published in reference textbooks [26,27]. Commercial phosphor TLD-100 was used to compare the performance of the material. TLD-100 in powder form was used.

3. Results

Figure 1a shows the FTIR spectrum as a function of incorporating NaF in the barium borate glass. The FTIR spectrum of borate glasses showed a characteristic pattern; one band in the region 500–800 cm^{-1} , which is related to the vibration of B–O–B linkage [28], another in the region 800–1150 cm^{-1} , and a last band in the 1150–1550 cm^{-1} range, associated with BO_4 and BO_3 species, respectively [28,29]. The deconvoluted signal was used to interpret the spectra for all samples. The area under the curve, corresponding to BO_3 and BO_4 species, was used to evaluate the four-fold fraction (N_4) (Figure 1b). The N_4 value increased as the concentration of NaF increased. Figure 1c shows the Raman spectra for all samples, as it was possible to observe the following main bands at: ~ 490 , ~ 760 , ~ 950 , ~ 1110 , and ~ 1300 – 1450 cm^{-1} . The interpretation of FTIR and Raman spectra is shown in the discussion section, using previous data of glass and crystalline samples published elsewhere [30].

Figure 2 shows the density (ρ) as a function of the NaF concentration as it was possible to observe the density decrease as the NaF concentration increased.

Figure 3a shows the variation of the DSC signal as the concentration of NaF increased, while Figure 3b shows the variation of T_g according to the NaF concentration. The value of T_g decreased as the concentration of NaF increased. A sample with $x = 0\%$ showed one peak corresponding to the crystallization of $\text{BaO}\cdot 2\text{B}_2\text{O}_3$. With the incorporation of NaF (up to $x = 15\%$), the DSC peak showed some modifications. The peak (identified as A in Figure 3a) became wider and shifted to a higher temperature. For the sample containing $x = 20\%$, two peaks appeared, one of them at the same temperature range of the peak of $x = 15\%$ and the other at a lower temperature (peak identified as B). With the increase in the NaF concentration, another peak, which was identified as C, began to gain importance (see Supplementary Materials for a detailed view). To analyze the effect of the incorporation of NaF on the glass crystallization, representative bulk samples were subject to a programmed heat-treatment. The results of these experiments are shown in Figure 3c.

According to XRD analysis, the sample with $x = 0\%$, which was heat-treated at 973 K for 60 min, showed the crystallization of BaB_4O_7 (COD #2310105). The sample containing 15% NaF, heat-treated at 921 K for 30 min, and the sample with $x = 20\%$ NaF, heat-treated at 873 K for 30 min, showed the crystallization of $\text{Ba}_4\text{B}_{11}\text{FO}_{20}$ (COD #4119492). Meanwhile, the sample with 35% NaF, heat-treated at 723 K for 15 min, showed the crystallization of BaF_2 (COD #9009004), and some peaks could be identified as NaF (COD #9008679). To go deeper in the analysis of crystallization, we performed a kinetic analysis, and the results of this analysis are shown in Figure 3d. As it is possible to observe from the plot, there was a shift of the slope, which corresponded to a variation in the activation energy for crystal growth.

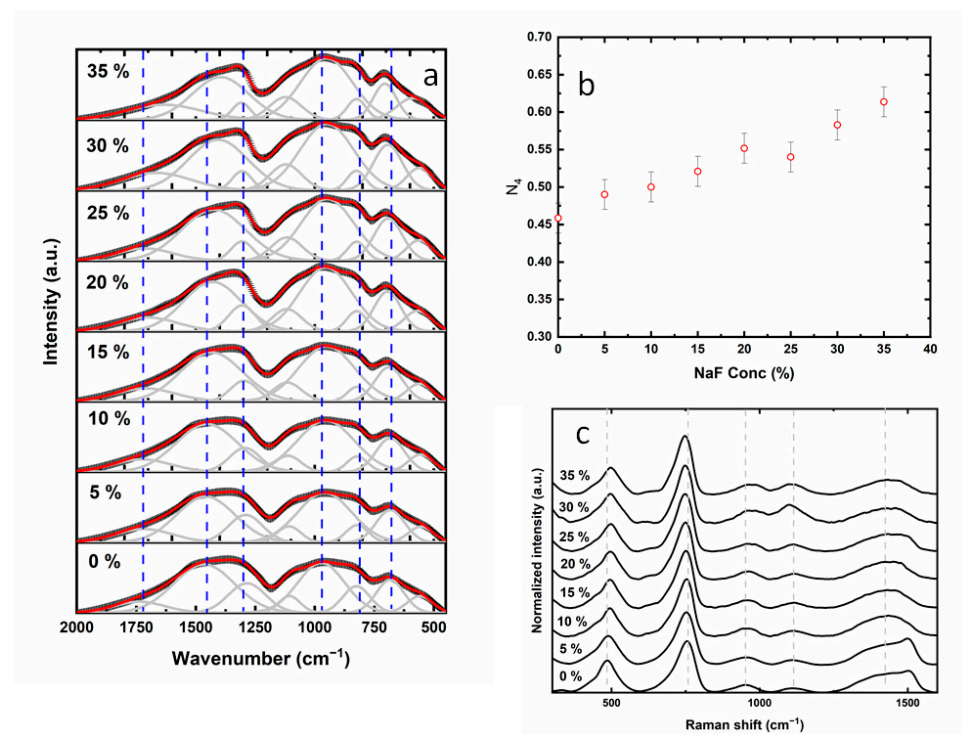


Figure 1. (a) FTIR experimental data are indicated with crosses, the convoluted bands are indicated in gray, and the adjusted spectrum is indicated in red. The blue shaded lines are to aid in visualization. (b) Evolution of the N_4 fraction as a function of the NaF concentration with the corresponding error bars. (c) Raman spectra of the samples studied. Intensity was normalized, with respect to 760 cm^{-1} band maximum, for better visualization. The gray shaded lines are to aid in visualization.

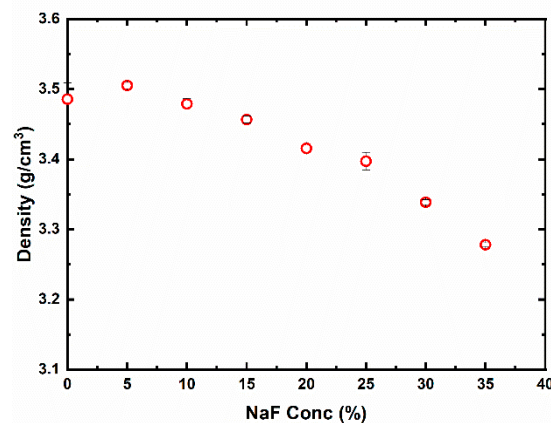


Figure 2. Variation of room temperature density measurements as a function of NaF concentration.

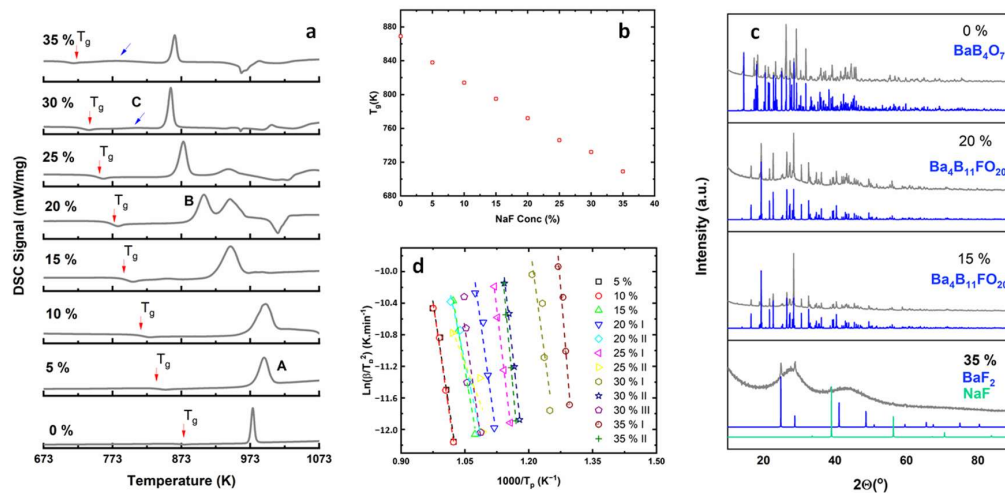


Figure 3. (a) DSC signal as a function of NaF concentration. Red arrows indicate the value of T_g for visualization. Blue arrows indicate the wider peak identified as C. (b) Variation of T_g as a function of NaF concentration. (c) XRD diagram for different samples heat-treated at different temperatures. Blue indicates the identified crystalline phase. (d) Kinetic analysis of crystallization for different samples.

Figure 4 shows the main results of the TL analysis. Figure 4a,b show the variation of the TL glow curve with the irradiated dose for glass samples containing 0% and 20% NaF. It is possible to observe an increase in the maximum intensity of the TL curve with the irradiation dose for both types of samples. The same effect was observed for other samples (all glow curves were included in the Supplementary Materials for better visualization). Figure 4c shows the intensity modification with the varied irradiated dose for all studied samples. For all samples, a linear behavior was observed with the irradiation dose. Additionally, the variation of the maximum intensity as the concentration of NaF varied, $x = 20\%$ being the sample that gives the highest signal. The maximum intensity of the TL curve was plotted as a concentration function of NaF in Figure 4d to observe this effect better.

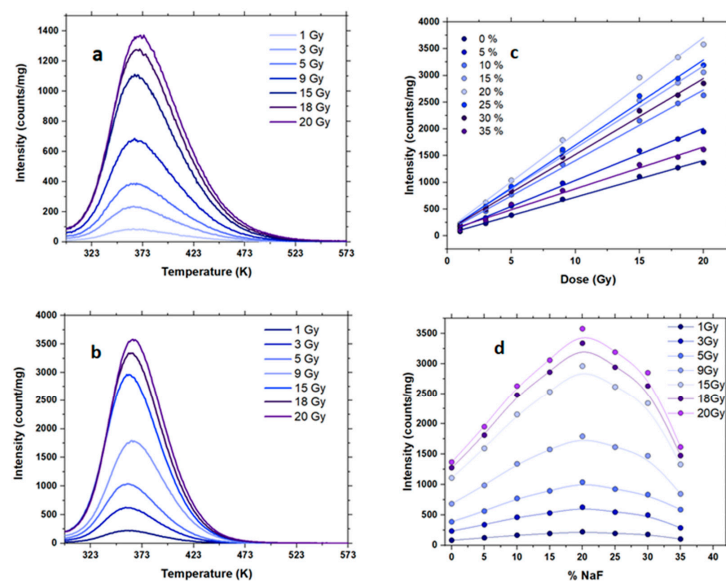


Figure 4. (a) Sample with $x = 0\%$ irradiated at different irradiation doses. (b) Representative sample with $x = 20\%$ irradiated at different irradiation doses. (c) Intensity as a function of different irradiation doses for different samples. (d) Variation of the intensity as a function of different concentrations of NaF for different irradiated samples.

To interpret and analyze the kinetic of the TL glow curve, we used a different approach found in the literature. First, we analyzed the variation of the temperature of the peak maximum (T_M). From Figure 4a,b, it is possible to observe that the T_M remains unchanged as the irradiation dose increases, which could be consistent with first-order kinetics [31]. The same effect was observed for other samples (Supplementary Electronic Materials). To test the reaction order, we used the shape method [26,32]. In this method, few parameters were used: The T_M , the temperature of the left side at half the height of the peak maximum, T_1 , the temperature of the right side at half the height of the peak maximum, T_2 , and the parameters; $\omega = T_2 - T_1$ (the total width), $\delta = T_2 - T_M$, $\tau = T_M - T_1$, and the symmetry factor, $\mu = \delta/\omega$ [26]. It is well known that, for the first order, $\mu = 0.42$, meanwhile for second order, $\mu = 0.52$. In Table 1, it is possible to observe the results of average μ at different doses. To obtain the value of the activation energy, we used the initial rise method [32]. The results of this calculation are also shown in Table 1.

Table 1. Average results for samples irradiated at different irradiation dose. μ : peak shape factor, E_a : activation energy, IR: initial rise method, SO: second order. FOM: figure of merits.

NaF (%)	μ	E_a IR \pm 0.02 (Max Value)	E_a SO \pm 0.02 (Max Value)	R^2	FOM (%)
0	0.61	0.28	0.47	0.9898	5.5
5	0.58	0.30	0.52	0.9960	3.8
10	0.57	0.29	0.54	0.9970	3.4
15	0.57	0.28	0.57	0.9980	3.1
20	0.57	0.32	0.58	0.9980	3.4
25	0.57	0.33	0.60	0.9982	3.3
30	0.56	0.31	0.62	0.9986	2.9

Considering the value of the symmetry factor, it was possible to observe all samples showing values that were different from those corresponding to first-order kinetics. We used the peak fitting method to fit the corresponding peaks with second-order kinetics. The value obtained for activation energy and the figure of merits (FOM) and the R^2 fitting parameters are also shown in Table 1. Despite the R^2 high value, the activation energy differs from those calculated with the initial rise technique. McKeever comments that, in the case of amorphous materials, defects occur over a range of values rather than only one value and that the shape of the TL glow curve seems to be second-order [26]. The T_m - T_{stop} method was applied to verify that these samples could be interpreted as second-order kinetics [33]. Figure 5 shows the main results of the applied method. Figure 5a,c shows the curves as a function of the stop temperature, T_{stop} , (varying from 50 to 150 °C) for $x = 0\%$ and $x = 20\%$ samples. From these plots, it is possible to observe that, as the T_{stop} increased, the peak shifted to a higher temperature and the intensity decreased. In the case of $x = 0\%$, a shoulder was observed as the T_{stop} increased. The activation energy for each curve was evaluated using the initial rise technique to analyze this effect, as shown in Figure 5b,d. The results of activation energy found for $x = 0$ and $x = 20\%$ are shown in Figure 5f,g. Gaussian distribution of traps was observed for both cases. Other distributions were tested, but the quality of the fitting was not good. In Figure 5e, the plot of the T_M - T_{stop} method is shown, indicating a linear behavior, which McKeever considered a quasi-continuous distribution of peaks [33].

Figure 6 shows the comparison of the TL signal of $x = 20\%$ with commercial phosphor TLD-100. The same conditions of measurements of glass samples was used.

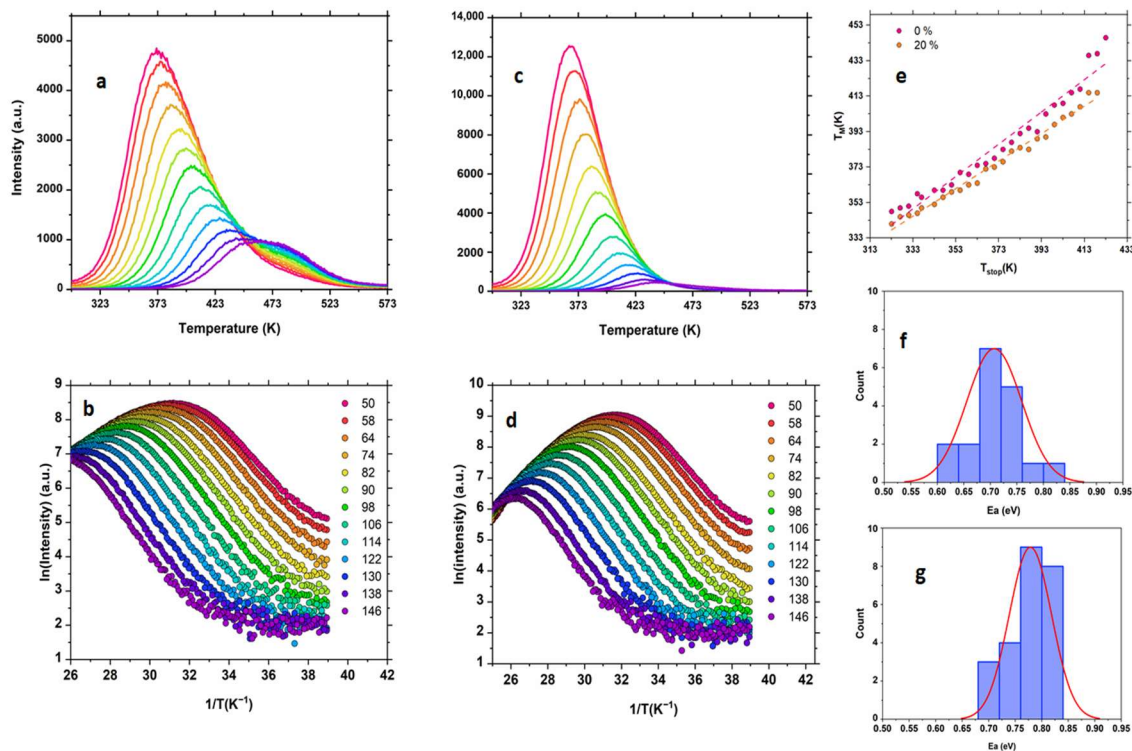


Figure 5. (a) Application of T_M - T_{stop} for $x = 0\%$ and (b) initial rise method applied for $x = 0\%$ samples. For clarity, selected temperatures were plotted. The temperature variation was 4 K. (c) Application of T_M - T_{stop} for $x = 20\%$ and (d) initial rise method applied for $x = 20\%$. (e) T_M - T_{stop} for both samples. The linearity indicates a continuous trap distribution. (f,g) Representative distribution of the activation energy obtained in the initial rise method, respectively.

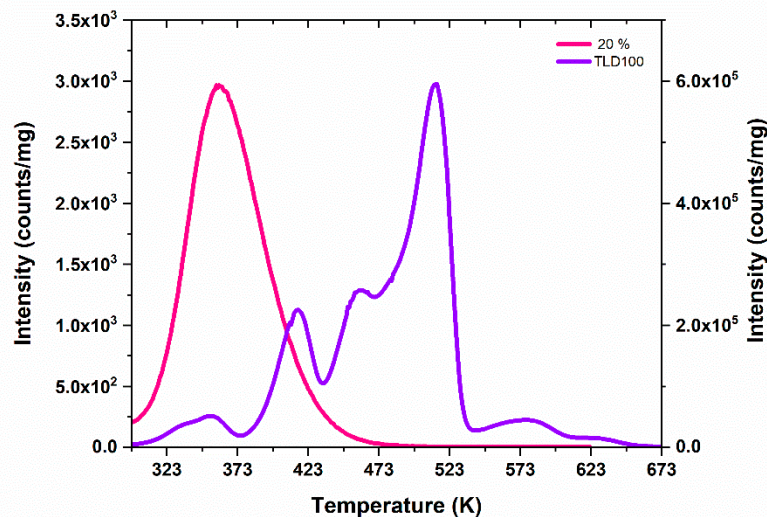


Figure 6. Comparison of the TL response of $x\text{NaF} (100 - x)\text{BaO} \cdot 2\text{B}_2\text{O}$ with $x = 20\%$ with the corresponding of the phosphor TLD-100.

4. Discussion

As was previously indicated, FTIR spectra of borate glasses show three main regions. Our results for the $x = 0\%$ sample indicated three main bands near ~ 1452 , ~ 972 , and $\sim 683 \text{ cm}^{-1}$ (indicated with a blue shaded line). As the content of NaF increased, these bands showed slight modifications. For example, for $x = 35\%$, the three main bands appeared near ~ 1395 , ~ 950 , and 705 cm^{-1} . The other bands showed similar behavior.

For example, bands at ~ 1634 , ~ 1395 , ~ 1123 , ~ 825 , and ~ 589 cm^{-1} shifted to ~ 1737 , ~ 1284 , ~ 1105 , ~ 824 , and ~ 558 cm^{-1} , respectively, as the concentration of NaF increased.

The structure of the crystalline phase of $\text{BaO}\cdot 2\text{B}_2\text{O}_3$ indicated that a borate network of single and double rings, linked by oxygen and containing boron with three and four coordination exists [34]. This structure does not contain non-bridging oxygen [35] and contains half of the boron in BO_3 species and the other half in BO_4 species [36]. The possible super-structural units are di-pentaborate group and di-triborate group [37]. The FTIR spectra of crystalline $\text{BaO}\cdot 2\text{B}_2\text{O}_3$ showed the main absorption band at 1340 cm^{-1} due to B-O symmetric stretching of BO_3 species, at 1030 cm^{-1} and 930 , assigned to the B-O stretching of BO_4 species in di-triborate and dipentaborate groups [35]. Meanwhile, the structural model for glasses of composition $\text{MO}\cdot 2\text{B}_2\text{O}_3$ ($x_M = 0.33$) indicated that the structure was composed of diborate, di-pentaborate, and di-triborate super-structural units [37].

To analyze the spectra and assign the deconvolved bands, a comparison was made with previously published data for crystalline phases and glasses. For example, the spectrum of crystalline lithium diborate presents bands at 982 and 1390 cm^{-1} , and, since its structure presented diborate groups, we can say that the band observed in our glass at ~ 972 cm^{-1} can be associated with the diborate group [38]. $\text{Li}_2\text{O}\cdot 3\text{B}_2\text{O}_3$ crystalline, consisting mainly of tri-borate super-structural units, shows bands at ~ 1000 cm^{-1} [38]. Pentaborate and triborate groups show bands at ~ 1275 cm^{-1} , and metaborate shows bands at ~ 1400 cm^{-1} [38]. From the reported bands, deconvolved bands at 972 and 1325 cm^{-1} could be associated with the presence of diborate. The region of 1200 – 1500 cm^{-1} could be associated with B-O stretching vibration of BO_3 units, which possess bridging and non-bridging oxygen ions, such as metaborate [39].

On the other hand, the incorporation of NaF produces a modification of the network [40]. For example, in glasses of composition $x\text{BaF}_2\cdot(100-x)\text{B}_2\text{O}_3$, an increase in the N_4 value was observed. This N_4 value increase was interpreted as the increase of the $[\text{BO}_3\text{F}]^-$ species (in other words B tetrahedral species) [41]. In another work, it was indicated that a band at ~ 1000 cm^{-1} was due to the formation of $[\text{BO}_3\text{F}]^-$ [42]. Taking this into account, it is possible to interpret that the incorporation of NaF in our $\text{BaO}\cdot 2\text{B}_2\text{O}_3$ glass produced a modification of the network, appearing species-like $[\text{BO}_3\text{F}]^-$. The increase in bands in the region 800 – 1150 cm^{-1} could be associated with this species formation. The analysis of the variation of N_4 as the concentration of NaF increases (Figure 1b) indicates the increase of B_4 species, which was also observed in other glass systems [39,43–45]. Table 2 summarizes the main band assignments. The increase in the band relative to 1634 cm^{-1} as the NaF content increased indicates that the glass showed a more depolymerized structure.

Table 2. FTIR main band assignments for different $x\text{NaF}\cdot(100-x)\text{BaO}\cdot 2\text{B}_2\text{O}_3$ glass samples.

Frequency Bands (cm^{-1})	Bands Assignment	References
589	B–O–B bending vibration in the borate network	[29]
683	pentaborate group	[38]
825	B–O stretching vibration in BO_3 species	[29]
950	diborate group	[38]
1080	BO_3 species/ $[\text{BO}_3\text{F}]^-$	[42]
1125	pentaborate group	[38]
1395–1452	B–O stretching vibration in BO_4 species	[29]

The Raman spectra showed similar behavior. As the concentration of NaF increased, some relative band intensities showed modifications (for example, those at 480 and 1100 cm^{-1}), and there was shape modification of the envelope in the 1200 – 1600 cm^{-1} region. The absence of a significant modification, such as the disappearance of one band or the appearance of another, indicates that the overall structure of these samples showed slight variations. The shape variations of envelopes in the region 1200 – 1600 cm^{-1} indicate

a decrease in the component over 1500 cm^{-1} as the NaF content increased. In turn, there was an increase in the intensity of the 1100 cm^{-1} and 480 cm^{-1} bands.

Previous reports show that bands at 485, 755, and 930 cm^{-1} indicate the presence of pentaborate or di-pentaborate super-structural groups [46]. The presence of bands at 1150 cm^{-1} indicate the existence of diborate groups [46]. The band at 490 cm^{-1} , which was associated with $[\text{B}\emptyset_4]^-$ tetrahedra (\emptyset corresponds to bridging oxygen atoms), appears in glasses of the composition $x\text{BaO}\cdot(100-x)\text{B}_2\text{O}_3$ with $x = 20\text{--}50\%$ [47]. Additionally, it was reported that bands at 1460 cm^{-1} correspond to asymmetric $\text{B}\emptyset_2\text{O}^-$ triangles [47]. Bands at 500, 757, and 1490 cm^{-1} were associated with the presence of $[\text{BO}_3\text{F}]^-$ structure, while a band at 600 cm^{-1} was associated with the presence of $[\text{BO}_2\text{F}_2]^-$ [48].

Based on the above, we can assign the bands as follows: the band at $\sim 490\text{ cm}^{-1}$ could be associated with $[\text{B}\emptyset_4]^-$ tetrahedra, $\sim 760\text{ cm}^{-1}$ could be associated with triborate groups, $\sim 950\text{ cm}^{-1}$ could be associated with diborate groups, $\sim 1100\text{ cm}^{-1}$ could be associated with pentaborate groups, and the band at $\sim 1460\text{ cm}^{-1}$ could be associated with $\text{B}\emptyset_2\text{O}^-$ triangles. The small band at 600 cm^{-1} , the deformation of the $600\text{--}800\text{ cm}^{-1}$ band, and the relative increase of the 1490 cm^{-1} band with the NaF concentration can be related to the existence of $[\text{BO}_3\text{F}]^-$ and $[\text{BO}_2\text{F}_2]^-$ structures. These structures may increase the N_4 value.

The identification of these groups in the Raman spectra is consistent with what was found in the FTIR spectra, and the possible existence of tetrahedral structures of B-O-F indicate that the increase in N_4 would be confirmed from these results.

The density of $\text{BaO}\cdot 2\text{B}_2\text{O}_3$ glass was reported as 3.411 g/cm^3 [49], meanwhile, the crystalline phase was reported as 3.57 g/cm^3 [34,50]. Our room temperature measurement of density was 3.49 g/cm^3 for $x = 0\%$ sample. As the concentration of NaF increases, density decreased. The incorporation of NaF to $\text{BaO}\cdot 2\text{B}_2\text{O}_3$ glass produced a decrease in the molar volume (passing from 28.0 to $23.8\text{ cm}^3/\text{mol}$), considering that a lighter compound was introduced into the composition. On the other hand, it is well known that there is a relation between the density and the N_4 fraction for borate glasses [51,52]. The value of N_4 and the density are maximum for glasses with composition $x = 0.33$. With non-bridging oxygen ions (NBOs) appearing in the structure, the N_4 and the density diminish. From our FTIR results, it is possible to conclude that N_4 increased as the NaF content increased, and therefore, we would expect an increase in density. However, when the NaF content increased, the molar volume decreased, since it became a lighter structure. This last effect became more pronounced, and therefore, a decrease in density was observed. The same effect was observed when Na_2O was substituted by NaF in gadolinium phosphate glasses [53].

According to DSC results, the crystallization of $\text{BaO}\cdot 2\text{B}_2\text{O}_3$ glass showed a peak whose T_c is 972 K . the existence of a fine and high peak indicates that crystallization occurred rapidly from glass particles. Previous reports indicated a T_c of 968 K [54]. With the addition of NaF, there was a variation both in the maximum peak's shape and the temperature. Considering that a greater nuclei density would imply a more significant heat release, it would be detected at a lower temperature in a DSC-DTA experiment [55]. Additions of NaF to the glass matrix produce an increase in the number of nuclei densities. At $x = 20\%$, the appearance of a second peak (identified as B in Figure 3) indicates that the crystallization occurred in two steps with different crystalline phases. The same effect, the appearance of two nearby crystallization peaks, was observed during the crystallization of CaSiO_3 and CaB_2O_4 in $\text{CaO}\text{--}\text{B}_2\text{O}_3\text{--}\text{SiO}_2$ glasses [56]. To evaluate which crystalline phase was crystallizing, after verifying the amorphous state of all the glass samples by XRD, several crystallization experiments were designed and performed. For this, different glass pieces polished to optical quality (to diminish the effect of heterogeneous crystallization on the surface) were heat-treated at temperatures nearby T_c temperatures for different times. In the particular case of the sample with $x = 0\%$, it was observed that the crystalline phase developed corresponded to BaB_4O_7 . Therefore, the NaF addition generated some modification of the network structure (this modification was observed in modifications of the measured parameters, such as T_g , density, FTIR, and Raman spectroscopy), which became observable above $x = 20\%$ and manifested itself through a separation in two

crystallization events. In these cases, the first crystalline phase developed corresponded to the $\text{Ba}_4\text{B}_{11}\text{FO}_{20}$ crystalline phase. As the amount of NaF increased, the peak shifted towards lower temperatures, and only at $x = 30\%$ a new broader peak appeared (identified as C in Figure 3a), which corresponded to the crystallization of a fluoride phase, as confirmed by XRD analysis. Two other crystallization events occurred at higher temperatures. Similar results regarding the decrease in T_g in doped samples were previously published [57].

A kinetic study of crystallization was carried out in order to obtain information on the crystallization mechanism. There are several methods for performing kinetic analysis [58,59], and there are reports that analyze the validity of the results obtained by these methods [55]. Here, we used the Kissinger method to obtain the overall effective activation energy for crystallization ($E_{a,cr}$), which corresponds to the sum of the activation energy for nucleation and crystal growth. Some of the limitations of this technique were widely discussed in [59]. Moreover, under the assumption that the nucleation frequency is negligible in the temperature range of the study, this activation energy corresponds to the activation energy for crystal growth [58]. The activation energy for crystal growth of $\text{BaO}\cdot 2\text{B}_2\text{O}_3$ was previously published [21,50]. In Figure 7 the values of $E_{a,cr}$ obtained are plotted. As it is possible to observe, we classified its value according to the following criteria. Samples containing $x < 25\%$ showed an $E_{a,cr}$ with an average value of 341 kJ/mol (identified as I in the plot). This $E_{a,cr}$ corresponded to peaks in the higher temperature range (identified as peaks A and B in Figure 3a), which was associated principally with the crystallization of $\text{Ba}_4\text{B}_{11}\text{FO}_{20}$. The second type of $E_{a,cr}$ was identified as II in Figure 7, which corresponded to peaks with higher temperature range (the second peak in the DSC signal of $x = 20\%$ and $x = 25\%$ in Figure 3B); meanwhile, the third type (identified as III), with an average value of 481 kJ/mol, corresponded to the crystallization of the fluoride phase. The decrease in the value of type II could be understood as an activation energy of heterogeneous crystallization.

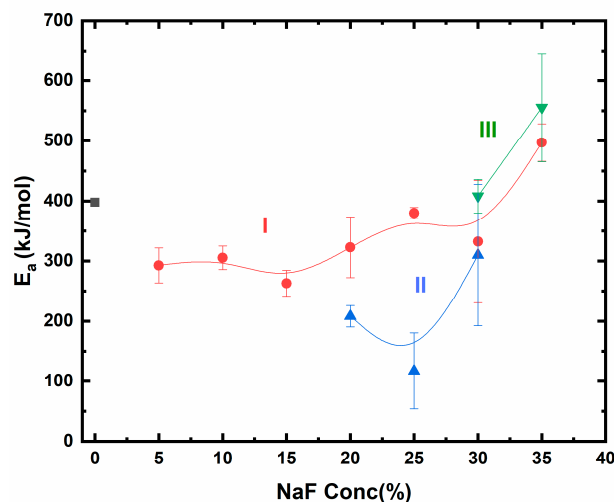


Figure 7. The activation energy of crystal growth for different crystalline phases observed in Figure 3a.

The crystal growth depends on the inverse of the viscosity. In oxyfluoride silicate glasses, a variation in the composition at the interface produces an increase in viscosity. Thus, the growth of the crystals is limited, observing a homogeneous distribution of nanocrystals [60] and distribution of dopants inside the phase separate droplets [61]. However, the viscosity of oxyfluoro borate melt is lower [62]. For this reason, some authors suggest that such a diffusion barrier should not be expected to exist [20]. The results obtained in the present work show that the value obtained for the activation energy was similar to the value obtained in the crystallization of BaF_2 in silicate glasses [63,64]. On the other hand, previous results on borates indicate that the crystallization depends on the nature of the cation modifier and fluoride compound [45]. Although it is necessary to

deepen the study of crystallization in these systems, it could be speculated that, depending on the activation energy values obtained being similar to silicate glasses, the process could be similar. In other words, during the crystallization of these oxyfluoroborates, a phase separation would first occur, which limits crystallization. The difference in the enthalpy of fusion (ΔH_f) between some of the possible intervening species (NaF: -576.6 , BaF₂: -1207.1 , Na₂O: -414.2 , BaO: -548 all in kJ/mol) would indicate the formation preference of certain types of compounds, such as BaF₂ [65], affecting the nucleation rate. Therefore, an increase in the nucleation rate and a decrease in the crystal growth rate due to increased viscosity would allow a uniform distribution of nanocrystals to be obtained. It would be necessary for the phase separation to include the greatest amount of fluorine and thus lower the viscosity even more.

As was previously introduced, all glasses showed an increase in the TL signal as the irradiation dose increased. In the $x = 0\%$ case, a peak centered at ~ 370 K was observed. The increase in the TL signal with the irradiation dose and the effect of its crystallization were previously studied [21]. In crystalline samples, one intense peak was observed at 468 K when samples were heated at 1°C/s [66]. Because of the different heating rates used in our work, a direct comparison is not possible. Considering that higher heating rates shift the peaks to higher temperatures, they should appear at higher temperatures if other peaks exist in our samples. However, due to the possibility of flowing samples at temperatures close to the T_g , our maximum working temperature was limited, and this peak was not observed. At first glance, the TL glow curve appeared to be made up of a single peak. Since the temperature of the maximum (T_M) of the intensity did not vary considerably, it suggests first-order kinetics. To verify this, we analyzed the shape of the curve by analyzing the width of the TL glow curve. The average results of the parameter μ for different irradiation doses shown in Table 1 indicate that this value was higher for first-order kinetics. We also used the fitting method to evaluate the first-order kinetics. The high value obtained from the FOM parameter confirmed that the samples followed another kinetic order. We used the IR method to characterize the E_a , since this method does not depend on the kinetic order, and in the analyzed region of temperature, the number of trapped electrons could be constant [32]. The values are relatively low compared to typical thermoluminescent materials [5]. A second-order kinetic was also tested. The peak fitting method was used, and the FOM and R^2 parameters were used as criteria for the fitting. The fitting was improved compared to first order (Table 1). Considering what was mentioned about the existence of more than one peak for crystalline samples [66], we used the T_M - T_{stop} method. The results of this are shown in Figure 5e. The continuous increase in the T_M with T_{stop} indicates a continuous trap distribution [33]. Various types of distribution were used to explain this type of effect in glasses [67]. The results obtained here indicate a Gaussian distribution of the value of the activation energy. For the case of $x = 0\%$, the value was around 0.75 ± 0.04 eV; meanwhile, for $x = 0.20\%$, the value was around 0.78 eV ± 0.04 . These results are consistent with our previous results of Nd³⁺ doped oxyfluoride glass [25].

When NaF was incorporated into the structure, the peak underwent some modifications. In particular, it became narrower and increased in intensity to a concentration of $x = 20\%$, then the signal decreased (Figure 8). The temperature where the peak maximum occurred shifted to lower values, indicating the participation of Na and F in the TL mechanism.

It is well known that broken silicon and oxygen bonds (called non-bridging oxygen (NBO)) are typical defects present in Quartz and act as hole traps, while empty Si orbitals act as electron traps [27]. In the case of glasses of the system Li₂O-B₂O₃, previous reports indicate an increase in the TL intensity as the concentration of Li₂O increases until it reaches 50%, and after, it decreases [7]. According to the actual structural model for alkali glasses, the composition with $x = 33\%$ presents the highest content of BO₄ species, and higher Li₂O content produces an increase in the quantity of NBO [37]. According to McKeever, the increase in the NBO should produce an increase in the TL signal [27]. However, the TL of

$\text{Li}_2\text{O}-\text{B}_2\text{O}_3$ glasses decreases at higher Li_2O content, and it is not possible to explain the trend in terms of the structural model or the NBO content.

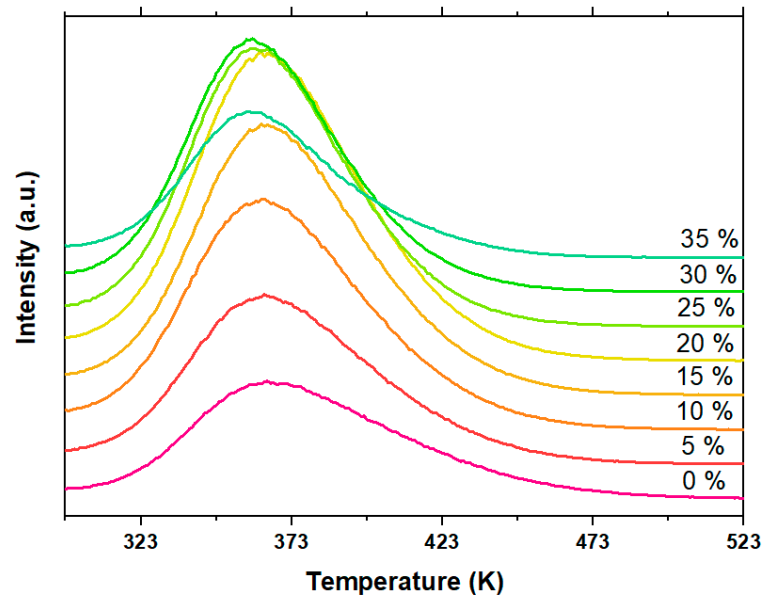


Figure 8. Variation in the peak shape of the TL glow curve for representative samples.

In our case, the increase in the amount of NaF produced an increase in the amount of N_4 by the formation of $[\text{BO}_3\text{F}]^-$ and $[\text{BO}_2\text{F}_2]^-$, which indicates an increase in the TL signal. However, for values greater than $x = 20\%$, a decrease in the TL signal was observed. On the other hand, it is known that the substitution of NaO by NaF produces a shift towards lower wavelengths of the cut-off energy in the absorbance spectrum, which would be a greater band gap [40]. The above-mentioned would suggest that structural modifications produced a higher band gap, increasing the number of possible defects, and therefore, a greater number of traps could be generated. If this were the case, there would be an increase in the number of traps with the increase in the amount of NaF, and therefore, it would be possible that a quenching effect would be observed. This would explain a decrease in the number of traps as it increases above $x = 20\%$ NaF. From the structural point of view, it would be a more open network (as indicated by the results of FTIR, Raman, and T_g), and therefore, with a greater number of defects, it also increased the charge imbalance, since 2 Na^+ replaced a Ba^{2+} ion.

Regarding the TL mechanism and considering that this system does not have dopants, everything would indicate that the species participating in the TL signal corresponds to metastable states located at oxygen vacancies of the glass matrix (Boron-Electron Center, BEC), bridging oxygen between a threefold-coordinated and fourfold-coordinated boron of the glass network (BOHC) [68] and the trapping sites, which could be barium, sodium, and other impurities present in the glass samples.

Despite its low performance compared to the commercial TLD-100, the possibility of controlling both the optical properties and the crystallization and obtaining glass-ceramics from these materials makes them promising materials for radiation sensors and spectral converters, among other applications.

5. Conclusions

Based on the results presented in this work on oxyfluoride glasses, we can conclude that, to obtain a material with adequate optical properties for use as a potential material for radiation detection, the addition of NaF to the barium borate glass matrix produces a substantial improvement. For this improvement to be considerable, 20% must be incorporated, which produces a structural modification and the appearance of the BaF_2 crystalline

phase during glass crystallization that could be used for the generation of nanoparticles suitable for doping. The distribution of existing defects in the glass would indicate that they follow a continuous distribution of Gaussian-type traps with E_a values close to 0.8 eV, which makes this material promising for use as a radiation sensor or in spectral converters.

Supplementary Materials: New Perspective on Thermally Stimulated Luminescence and Crystallization of Barium Borate Oxyfluoride Glasses - Supplementary Materials The following are available online at <https://www.mdpi.com/article/10.3390/cryst11070745/s1>, Figure S1: Differential scanning calorimetry of $x\text{NaF}\cdot(100 - x)\text{BaO}\cdot 2\text{B}_2\text{O}_3$ samples with $x = 30$ and 35% . Figure S2: Thermoluminescence response for different samples $x\text{NaF}(100 - x)\text{BaO}\cdot 2\text{B}_2\text{O}_3$ with $x = 0, 5, 10, 15, 20, 25, 30, 35\%$ (in mol) irradiated at different doses.

Author Contributions: Conceptualization, methodology, formal analysis, and writing—original draft preparation; M.R.C.; formal analysis, G.A., H.B.P. and R.F.; review and editing, M.R.C., G.A., H.B.P. and R.F. All authors have read and agreed to the published version of the manuscript.

Funding: This work was supported by the “Comisión Sectorial de Investigación Científica” (CSIC), Uruguay and the “Programa de Desarrollo de Ciencias Básicas” (PEDECIBA), Uruguay.

Institutional Review Board Statement: Not applicable.

Informed Consent Statement: Not applicable.

Data Availability Statement: Not applicable.

Acknowledgments: The authors thank the use of the TL and other equipment of the Laboratorio de Alta Complejidad, Centro Universitario Regional del Este (CURE).

Conflicts of Interest: The authors declare no conflict of interest. The funders had no role in the design of the study; in the collection, analyses, or interpretation of data; in the writing of the manuscript, or in the decision to publish the results.

References

1. Azorin, J. Preparation methods of thermoluminescent materials for dosimetric applications: An overview. *Appl. Radiat. Isot.* **2014**, *83*, 187–191. [[CrossRef](#)]
2. Bos, A.J.J. Thermoluminescence as a Research Tool to Investigate Luminescence Mechanisms. *Material* **2017**, *10*, 1357. [[CrossRef](#)] [[PubMed](#)]
3. Jain, M.; Kumar, R.; Won, S.O.; Chae, K.H.; Vij, A.; Thakur, A. Manju Defect states and kinetic parameter analysis of ZnAl_2O_4 nanocrystals by X-ray photoelectron spectroscopy and thermoluminescence. *Sci. Rep.* **2020**, *10*, 1–14. [[CrossRef](#)] [[PubMed](#)]
4. Murthy, K. Thermoluminescence and its Applications: A Review. *Defect Diffus. Forum* **2013**, *347*, 35–73. [[CrossRef](#)]
5. Nieto, J.A. Present status and future trends in the development of thermoluminescent materials. *Appl. Radiat. Isot.* **2016**, *117*, 135–142. [[CrossRef](#)] [[PubMed](#)]
6. Kumar, D.; Rao, S.; Singh, S.P. Structural, optical and thermoluminescence study of Dy^{3+} ion doped sodium strontium borate glass. *J. Non. Cryst. Solids* **2017**, *464*, 51–55. [[CrossRef](#)]
7. Elkholly, M. Thermoluminescence of $\text{B}_2\text{O}_3\text{-Li}_2\text{O}$ glass System Doped with MgO . *J. Lumin.* **2010**, *130*, 1880–1892. [[CrossRef](#)]
8. Ekdal, E.T.; Ege, A.; Karali, T.; Townsend, P.; Prokić, M. Thermoluminescence studies of thermally treated $\text{CaB}_4\text{O}_7\text{:Dy}$. *Radiat. Meas.* **2010**, *45*, 764–767. [[CrossRef](#)]
9. Pimentel, N.; Mastelaro, V.; M'Peko, J.-C.; Martin, S.; Rojas, S.; De Souza, J. Structural and electrical characterization of glasses in the $\text{Li}_2\text{O-CaO-B}_2\text{O}_3$ system. *J. Non. Cryst. Solids* **2018**, *499*, 272–277. [[CrossRef](#)]
10. Isokawa, Y.; Hirano, S.; Kawano, N.; Okada, G.; Kawaguchi, N.; Yanagida, T. Dosimetric and scintillation properties of Ce-doped $\text{Li}_3\text{PO}_4\text{-B}_2\text{O}_3$ glasses. *J. Non. Cryst. Solids* **2018**, *487*, 1–6. [[CrossRef](#)]
11. Chialanza, M.R.; Castiglioni, J.; Fornaro, L. Crystallization as a way for inducing thermoluminescence in a lead borate glass. *J. Mater. Sci.* **2012**, *47*, 2339–2344. [[CrossRef](#)]
12. Tikhomirov, V.; Rodríguez, V.; Méndez-Ramos, J.; Del-Castillo, J.; Kirilenko, D.; Van Tendeloo, G.; Moshchalkov, V. Optimizing Er/Yb ratio and content in Er-Yb co-doped glass-ceramics for enhancement of the up- and down-conversion luminescence. *Sol. Energy Mater. Sol. Cells* **2012**, *100*, 209–215. [[CrossRef](#)]
13. Fedorov, P.; Luginina, A.; Popov, A. Transparent oxyfluoride glass ceramics. *J. Fluor. Chem.* **2015**, *172*, 22–50. [[CrossRef](#)]
14. Martin, A.D.P.; Durán, A.; Pascual, M.J. Nanocrystallisation in oxyfluoride systems: Mechanisms of crystallisation and photonic properties. *Int. Mater. Rev.* **2012**, *57*, 165–186. [[CrossRef](#)]
15. Bocker, C.; Avramov, I.; Rüssel, C. Viscosity and diffusion of barium and fluoride in $\text{Na}_2\text{O/K}_2\text{O/Al}_2\text{O}_3\text{/SiO}_2\text{/BaF}_2$ glasses. *Chem. Phys.* **2010**, *369*, 96–100. [[CrossRef](#)]

16. Martin, A.D.P.; Méndez-Ramos, J.; Del-Castillo, J.; Durán, A.; Rodríguez, V.; Pascual, M. Crystallization and up-conversion luminescence properties of Er³⁺/Yb³⁺-doped NaYF₄-based nano-glass-ceramics. *J. Eur. Ceram. Soc.* **2015**, *35*, 1831–1840. [CrossRef]
17. Pisarski, W.A.; Pisarska, J.; Dorosz, D.; Dorosz, J. Rare earths in lead-free oxyfluoride germanate glasses. *Spectrochim. Acta Part A Mol. Biomol. Spectrosc.* **2015**, *134*, 587–591. [CrossRef]
18. Ledemi, Y.; El Amraoui, M.; Ferrari, J.L.; Fortin, P.-L.; Ribeiro, S.; Messaddeq, Y. Infrared to Visible Up-Conversion Emission in Er³⁺/Yb³⁺ Codoped Fluoro-Phosphate Glass-Ceramics. *J. Am. Ceram. Soc.* **2013**, *96*, 825–832. [CrossRef]
19. Pisarski, W.A.; Pisarska, J.; Maczka, M.; Lisiecki, R.; Goryczka, T.; Dominiak-Dzik, G.; Ryba-Romanowski, W. Rare earth-doped lead borate glasses and transparent glass-ceramics: Structure–property relationship. *Spectrochim. Acta Part. A Mol. Biomol. Spectrosc.* **2011**, *79*, 696–700. [CrossRef]
20. Shinozaki, K.; Konaka, R.; Akai, T. Synthesis of new transparent borate-based BaF₂ nanocrystallized glass by formation of nucleation sites induced by rare earth ions. *J. Eur. Ceram. Soc.* **2019**, *39*, 1735–1739. [CrossRef]
21. Chialanza, M.R.; Keuchkerian, R.; Cárdenas, A.; Olivera, A.; Vazquez, S.; Faccio, R.; Castiglioni, J.; Schneider, J.; Fornaro, L. Correlation between structure, crystallization and thermally stimulated luminescence response of some borate glass and glass-ceramics. *J. Non. Cryst. Solids* **2015**, *427*, 191–198. [CrossRef]
22. Kissinger, H.E. Variation of peak temperature with heating rate in differential thermal analysis. *J. Res. Natl. Inst. Stand. Technol.* **1956**, *57*, 217. [CrossRef]
23. Koga, N.; Sestak, J. Crystal Nucleation and Growth in Lithium Diborate Glass by Thermal Analysis. *J. Am. Ceram. Soc.* **2004**, *83*, 1753–1760. [CrossRef]
24. Gražulis, S.; Chateigner, D.; Downs, R.T.; Yokochi, A.; Quirós, M.; Lutterotti, L.; Manakova, E.; Butkus, J.; Moeck, P.; Le Bail, A. Crystallography Open Database—An open-access collection of crystal structures. *J. Appl. Crystallogr.* **2009**, *42*, 726–729. [CrossRef] [PubMed]
25. Chialanza, M.R.; Azcune, G.; Pereira, H.B.; Gasparotto, G.; De Santana, R.C.; Maia, L.J.Q.; Carvalho, J.F. Continuous trap distribution and variation of optical properties with concentration in oxi-fluoroborate glass doped with Nd³⁺. *J. Non. Cryst. Solids* **2021**, *559*, 120683. [CrossRef]
26. Chen, R.; McKeever, S.W.S. *Theory of Thermoluminescence and Related Phenomena*; World Scientific: Singapore, 1997.
27. McKeever, S.W.S. *Thermoluminescence of Solids*; Cambridge University Press: Cambridge, UK, 1985.
28. Pisarski, W.A.; Pisarska, J.; Ryba-Romanowski, W. Structural role of rare earth ions in lead borate glasses evidenced by infrared spectroscopy: BO₃↔BO₄ conversion. *J. Mol. Struct.* **2005**, *744–747*, 515–520. [CrossRef]
29. Yiannopoulos, Y.D.; Chryssikos, G.D.; Kamitsos, E.I. Structure and properties of alkaline earth borate glasses. *Phys. Chem. Glas.* **2001**, *42*, 164–172. Available online: <http://www.ingentaconnect.com/content/sgt/pcg/2001/00000042/00000003/4203164> (accessed on 30 April 2021).
30. Kamitsos, E.I.; Patsis, A.; Chryssikos, G.D. Infrared reflectance investigation of alkali diborate glasses. *J. Non. Cryst. Solids* **1993**, *152*, 246–257. [CrossRef]
31. Bos, A. Theory of thermoluminescence. *Radiat. Meas.* **2006**, *41*, S45–S56. [CrossRef]
32. Pagonis, V.; Kitis, G.; Furetta, C. *Numerical and Practical Exercises in Thermoluminescence*; Springer: New York, NY, USA, 2006.
33. McKeever, S.W.S. On the analysis of complex thermoluminescence. Glow-curves: Resolution into individual peaks. *Phys. Status Solidi* **1980**, *62*, 331–340. [CrossRef]
34. Block, S.; Perloff, A. The crystal structure of barium tetraborate, BaO·2B₂O₃. *Acta Crystallogr.* **1965**, *19*, 297–300. [CrossRef]
35. Pernice, P.; Esposito, S.; Aronne, A.; Sigaev, V.N. Structure and crystallization behavior of glasses in the BaO–B₂O₃–Al₂O₃ system. *J. Non. Cryst. Solids* **1999**, *258*, 1–10. [CrossRef]
36. Block, S.; Perloff, A.; Weir, C.E. The crystallography of some M²⁺ borates. *Acta Crystallogr.* **1964**, *17*, 314–315. [CrossRef]
37. Wright, A.C. Borate structures: Crystalline and vitreous. *Phys. Chem. Glas. Eur. J. Glas. Sci. Technol. Part B* **2010**, *51*, 1–39. Available online: <http://www.ingentaconnect.com/content/sgt/pcg/2010/00000051/00000001/art00001> (accessed on 30 April 2021).
38. Kamitsos, E.I.; Patsis, A.; Karakassides, M.; Chryssikos, G.D. Infrared reflectance spectra of lithium borate glasses. *J. Non. Cryst. Solids* **1990**, *126*, 52–67. [CrossRef]
39. El-Egili, K.; Doweidar, H.; Ramadan, R.; Altawaf, A. Role of F[−] ions in the structure and properties of BaF₂B₂O₃ glasses. *J. Non. Cryst. Solids* **2016**, *449*, 83–93. [CrossRef]
40. Kamitsos, E.I.; Karakassides, M.A. A spectroscopic study of fluoride containing sodium borate glasses. *Solid State Ion.* **1988**, *28–30*, 783–787. [CrossRef]
41. Fan, H.; Hu, L.; Yang, K.; Fang, Y. Role of F[−] ions in the structure and properties of BaF₂-B₂O₃ glasses. *J. Non. Cryst. Solids* **2010**, *356*, 1814–1818. [CrossRef]
42. Maya, L. Crystalline Compounds and Glasses in the System B₂O₃-NaF-NaBF₄. *J. Am. Ceram. Soc.* **1977**, *60*, 323–328. [CrossRef]
43. Doweidar, H.; El-Damrawi, G.; Abdelghany, M. Structure and properties of CaF₂-B₂O₃ glasses. *J. Mater. Sci.* **2012**, *47*, 4028–4035. [CrossRef]
44. Doweidar, H.; El-Egili, K.; Altawaf, A. Structural units and properties of BaF₂-PbF₂-B₂O₃ glasses. *J. Non. Cryst. Solids* **2017**, *464*, 73–80. [CrossRef]
45. Chialanza, M.R.; Schneider, J.F.; Keuchkerian, R.; Romero, M.; Faccio, R.; Olivera, A.; Pereira, H.B. Structural analysis of oxyfluoride borate glass and BaF₂ crystallization from phase separation. *J. Am. Ceram. Soc.* **2020**, *103*, 3126–3137. [CrossRef]
46. Meera, B.; Ramakrishna, J. Raman spectral studies of borate glasses. *J. Non. Cryst. Solids* **1993**, *159*, 1–21. [CrossRef]

47. Osipov, A.A.; Osipova, L.M. Raman scattering study of barium borate glasses and melts. *J. Phys. Chem. Solids* **2013**, *74*, 971–978. [[CrossRef](#)]
48. Babushkina, O.; Voyiatzis, G.; Østvold, T.; Pakkanen, T.A.; Ahlgrén, M.; Pursiainen, J.; Wang, H.-G.; Yao, X.-K.; Tuchagues, J.-P.; Ogren, M. Raman and Infrared Spectroscopic Studies of (NaF–KF)–K₂MoO₄–B₂O₃ Melts and the Mechanism of Electrodeposition of Molybdenum. *Acta Chem. Scand.* **1999**, *53*, 320–328. [[CrossRef](#)]
49. Shartsis, L.; Shermer, H.F. Surface Tension, Density, Viscosity, and Electrical Resistivity of Molten Binary Al kaline-Earth Borates. *J. Am. Ceram. Soc.* **1954**, *37*, 545. [[CrossRef](#)]
50. Bergeron, C.G. Crystal growth kinetics in binary borate melts. In *Materials Science Research*; Pye, L.D., Fréchette, V.D., Kreidl, N.J., Eds.; Plenum Press: New York, NY, USA, 1978; Volume 12, pp. 445–462.
51. Doweidar, H.; El-Damrawi, G.; Moustafa, Y.; Ramadan, R. Density of mixed alkali borate glasses: A structural analysis. *Phys. B Condens. Matter* **2005**, *362*, 123–132. [[CrossRef](#)]
52. Karki, A.; Feller, S.; Lim, H.P.; Stark, J.; Sanchez, C.; Shibata, M. The density of sodium-borate glasses related to atomic arrangements. *J. Non. Cryst. Solids* **1987**, *92*, 11–19. [[CrossRef](#)]
53. Ravangvong, S.; Chanthima, N.; Rajaramakrishna, R.; Kim, H.; Kaewkhao, J. Effect of sodium oxide and sodium fluoride in gadolinium phosphate glasses doped with Eu₂O₃ content. *J. Lumin.* **2020**, *219*, 116950. [[CrossRef](#)]
54. Polyakova, I.G.; Pevzner, B.Z. Crystallization of barium diborate glass. *Glas. Phys. Chem.* **2005**, *31*, 138–144. [[CrossRef](#)]
55. Fokin, V.M.; Cabral, A.; Reis, R.M.; Nascimento, M.L.; Zanutto, E.D. Critical assessment of DTA–DSC methods for the study of nucleation kinetics in glasses. *J. Non. Cryst. Solids* **2010**, *356*, 358–367. [[CrossRef](#)]
56. Chang, C.-R.; Jean, J.-H. Crystallization Kinetics and Mechanism of CaO–B₂O₃–SiO₂ Glass-Ceramics. *J. Am. Ceram. Soc.* **1999**, *82*, 1725–1732. [[CrossRef](#)]
57. Chialanza, M.R.; Keuchkerian, R.; Gonçalves, T.S.; De Camargo, A.S.; Fornaro, L. The effect of cation modifier on improving the luminescent properties of borate glasses doped with Yb³⁺ and Er³⁺. *J. Non. Cryst. Solids* **2018**, *483*, 79–85. [[CrossRef](#)]
58. Yinnon, H.; Uhlmann, D. Applications of thermoanalytical techniques to the study of crystallization kinetics in glass-forming liquids, part I: Theory. *J. Non. Cryst. Solids* **1983**, *54*, 253–275. [[CrossRef](#)]
59. Vyazovkin, S.; Burnham, A.K.; Criado, J.M.; Perez-Maqueda, L.A.; Popescu, C.; Sbirrazzuoli, N. ICTAC Kinetics Committee recommendations for performing kinetic computations on thermal analysis data. *Thermochim. Acta* **2011**, *520*, 1–19. [[CrossRef](#)]
60. Bocker, C.; Wiemert, J.; Rüssel, C. The effect of viscosity on nanocrystallization of strontium fluoride from a silicate glass. *Solid State Sci.* **2014**, *30*, 55–60. [[CrossRef](#)]
61. Hoell, A.; Raghuvanshi, V.S.; Bocker, C.; Herrmann, A.; Rüssel, C.; Höche, T. Crystallization of BaF₂ from droplets of phase separated glass—evidence of a core–shell structure by SAXS. *Cryst. Eng. Comm.* **2020**, *22*, 5031–5039. [[CrossRef](#)]
62. Roth, M.; Perlov, D. Growth of barium borate crystals from sodium fluoride solutions. *J. Cryst. Growth* **1996**, *169*, 734–740. [[CrossRef](#)]
63. Sung, Y.-M. Crystallization kinetics of fluoride nanocrystals in oxyfluoride glasses. *J. Non. Cryst. Solids* **2012**, *358*, 36–39. [[CrossRef](#)]
64. Karmakar, P.; Subudhi, A.K.; Biswas, K.; Annapurna, K. Crystallization kinetics analysis of BaF₂ and BaGdF₅ nanocrystals precipitated from oxyfluoride glass systems: A comparative study. *Thermochim. Acta* **2015**, *610*, 1–9. [[CrossRef](#)]
65. John, A. Dean. In *Lange's Handbook of Chemistry*, 16th ed.; McGraw Hill Education: New York, NY, USA, 2017.
66. Yazici, A.N.; Dogan, M.; Kafadar, V.E.; Toktamış, H. Thermoluminescence of undoped and Ce-doped BaB₄O₇. *Nucl. Instrum. Methods Phys. Res. Sect. B Beam Interact. Mater. At.* **2006**, *246*, 402–408. [[CrossRef](#)]
67. Sakurai, T.; Shoji, K.; Itoh, K.; Gartia, R.K. Origin of the exponential distribution of traps in glass. *J. Appl. Phys.* **2001**, *89*, 2208–2212. [[CrossRef](#)]
68. Pontuschka, W.M.; Kanashiro, L.S.; Courrol, L. Luminescence Mechanisms for Borate Glasses: The Role of Local Structural Units. *Glas. Phys. Chem.* **2001**, *27*, 37–47. [[CrossRef](#)]